Tuning siRNA packing order in lipid nanoparticles modulates oligonucleotide functional delivery

Artu Breuer[# 1-3] Georgios Kyriakakis[# 1-3], Marcus W. Dreisler[1-4], Frank H. Schulz[1-3,5], Georgios Bolis[1-3], Stavroula Margaritaki[1-3], Vasilis Papageorgiou[1-3], Ntaniela Spacho[1-3], Nikos S Hatzakis*[1-3]

[1]Department of Chemistry & Nanoscience Center, University of Copenhagen, Copenhagen DK-2100, Denmark
[2]Novo Nordisk Foundation Center for Optimized Oligo Escape (COE), Department of Chemistry, University of Copenhagen, Frederiksberg DK-1870, Denmark
[3]Novo Nordisk Foundation Center for 4D cellular dynamics, Department of Chemistry, University of Copenhagen, Frederiksberg DK-1870, Denmark
[4]Department of Computer Science, University of Copenhagen, Copenhagen DK-2100, Denmark
[5]Sino-Danish Center for Education and Research (SDC), UCAS, China.

 # These authors contributed equally

Corresponding author: Nikos S Hatzakis hatzakis@chem.ku.dk.

Abstract

Efficient siRNA delivery by lipid nanoparticles (LNPs) is widely attributed to carrier composition, yet how intraparticle packing governs function remains unclear. Here, we developed a single-particle fluorescence microscopy assay that simultaneously quantifies size and siRNA loading of individual, chromophore-labeled LNPs. Imaging ~0.5M particles per hour uncovered two major packing modes: a high and a low order corroborated by cryo-EM. Quantitative live cell imaging on destabilized eGFP reporter cell line combined with systematic variation of LNPs lipid composition and N/P ratio allowed deconvolution of the interplay between siRNA packing, cell internalization and silencing and its dependance on lipid composition and electrostatics. Our findings surprisingly revealed that low-order particles while encapsulating modest RNA, they mediate more efficient knockdown of the destabilized eGFP reporter than their high-order counterparts. Guided by these findings we predicted and experimentally validated that tuning composition and N/P ratio to favor less compact siRNA packing enhances silencing

potency. This framework offers actionable guiding for the rational optimization of LNP formulations for RNA therapeutics.

Introduction

Lipid nanoparticles (LNPs) have revolutionized nucleic-acid therapeutics by enabling efficient systemic delivery of mRNA and siRNA, leading to the first approved mRNA vaccines against COVID-19[1]. Their clinical success arises from their compositional versatility in which ionizable lipids encapsulate and release cargo, phospholipids stabilize the structure, sterols regulate membrane packing and fluidity, and PEG-lipids reduce aggregation while extending circulation time. Yet, the same compositional diversity that supports adaptability across RNA modalities also complicates mechanistic interpretation. Despite intensive studies the physicochemical determinants of efficient endosomal escape and cytosolic delivery remain elusive.

Intracellular RNA delivery by LNPs is restricted by multiple barriers. Quantitative imaging shows that only ~1-5% of siRNA escapes into the cytosol following LNP uptake, with release confined to a limited endosomal window, showing escape as the principal bottleneck[2–6]. Time-resolved single-particle assays at endosomal membrane mimics reveal rapid acidification-driven disintegration events with heterogeneous, often partial cargo release, pointing to kinetic barriers beyond fusion[7]. Roughly 70% of internalized nucleic acid is exocytosed, decoupling uptake from functional delivery[8]. Membrane-damage markers such as Galectin recruitment indicates rupture but not necessarily productive RNA release, while ESCRT-mediated repair rapidly seals many lesions before escape can occur[9]. Thus, while endosomal rupture is necessary, they may not be sufficient for cytosolic nucleic-acid delivery, indicating that particle-intrinsic structural features, that to date remain portly understood, could determine the functional outcome.

The internal mesoscopic architecture of LNPs, defined by lipid composition, cargo identity, and N/P ratio, is intrinsically heterogeneous. Structural analyses by cryo-EM and SAXS reveal composition-dependent mesophase behavior[7,10–14], often modulated by N/P ratio: mRNA LNPs adopt pH-triggered inverse and non-lamellar phases[11], whereas siRNA LNPs remain lamellar, with RNA localized between apposed bilayers surrounding an amorphous lipid core[12,15,16]. The identity and molar fraction of the ionizable lipid, together with the N/P ratio, govern this internal order and balance encapsulation efficiency, membrane integrity, and potency[10,13]. Correlations between multilamellar-to-amorphous transitions and intracellular uptake and silencing have also been reported, yet these primarily relied on photoactivation to induce endosomal release[17] and provided clues on how lipid-siRNA organization regulates LNP responsiveness.

Phase organization is reported to influence delivery efficiency[18–24]. Conventional techniques such as dynamic light scattering and bulk fluorescence assays provide population-averaged readouts of LNP size and loading. These readouts mask due to ensemble averaging distinct subpopulations that differ in morphology and composition, thereby obscuring the nanoscale heterogeneity underlying functional diversity[19–22,25].Single particle studies offer a route to solve the intrinsic heterogeneity of LNP formulations. Li et al.[23] quantified size-payload variability by single-particle spectroscopic chromatography, revealing pronounced compositional dispersion yet without linking it to delivery efficacy. CryoEM studies showcased that inverse siRNA hexagonal phase enhances the intracellular silencing efficiency as compared to multilamellar phases[18]. Sjöberg et al.[24] combining scattering and fluorescence microscopy on supported lipid bilayers provided links of LNPs structural heterogeneity to loading and fusion. While these studies highlight the potential of single-particle methods to disentangle heterogeneity in morphology, loading, and dimensions, they do not provide direct links of heterogeneity to functional delivery.

Here, we developed a high-throughput single-particle fluorescence assay that simultaneously quantifies diameter and siRNA copy number for chromophore-labeled lipid nanoparticles (>0.5×10^6 particles per condition in less than 2 hours). This multimodal framework reveals two general packing orders, low-order and multilamellar high-order, that is validated structurally by cryo-EM. Our quantitative live-cell imaging of nanoparticle uptake and gene silencing quantified how packing mode modulates siRNA functional delivery. Systematic tuning of lipid composition and N/P ratio shifts the balance between the two packing states. Counterintuitively, low-order particles encapsulate modest amounts of siRNA yet mediate efficient cytosolic release and target knockdown, whereas high-order, cargo-rich particles remain inactive. By linking nanoscale organization to functional delivery at the single-particle level, this framework transforms LNP packing order into an actionable design parameter for RNA therapeutics.

Results

Platform for synchronous quantification of nanoparticle diameter and cargo loading at single-particle resolution

Quantitative characterization of lipid nanoparticles (LNPs) at the single-particle level is critical for understanding heterogeneity in formulation and delivery performance. Conventional methods such as Dynamic Light Scattering (DLS) and bulk fluorescence assays provide only ensemble averages[1,2], masking the heterogeneity of particle size and cargo loading, whereas existing single-LNP methods often depend on specialized or low-throughput instrumentation limiting their compatibility with standard fluorescence

microscopes[3-5]. To overcome these limitations, we established a generalizable single-particle fluorescence assay that integrates total internal reflection fluorescence (TIRF) microscopy with Gaussian-based particle analysis and calibration against DLS. This methodology, adapted from our earlier work on liposomes[26–29], allowed us to quantify the nanoscale dimensions of each diffraction limited LNP without the need for super resolution readout (Fig. 1a). This allows simultaneous measurement of LNP diameter and RNA cargo copy number with single-particle resolution, enabling analysis of >10^5 particles per condition (~10^6 across replicates), See Supplementary Fig. 1.

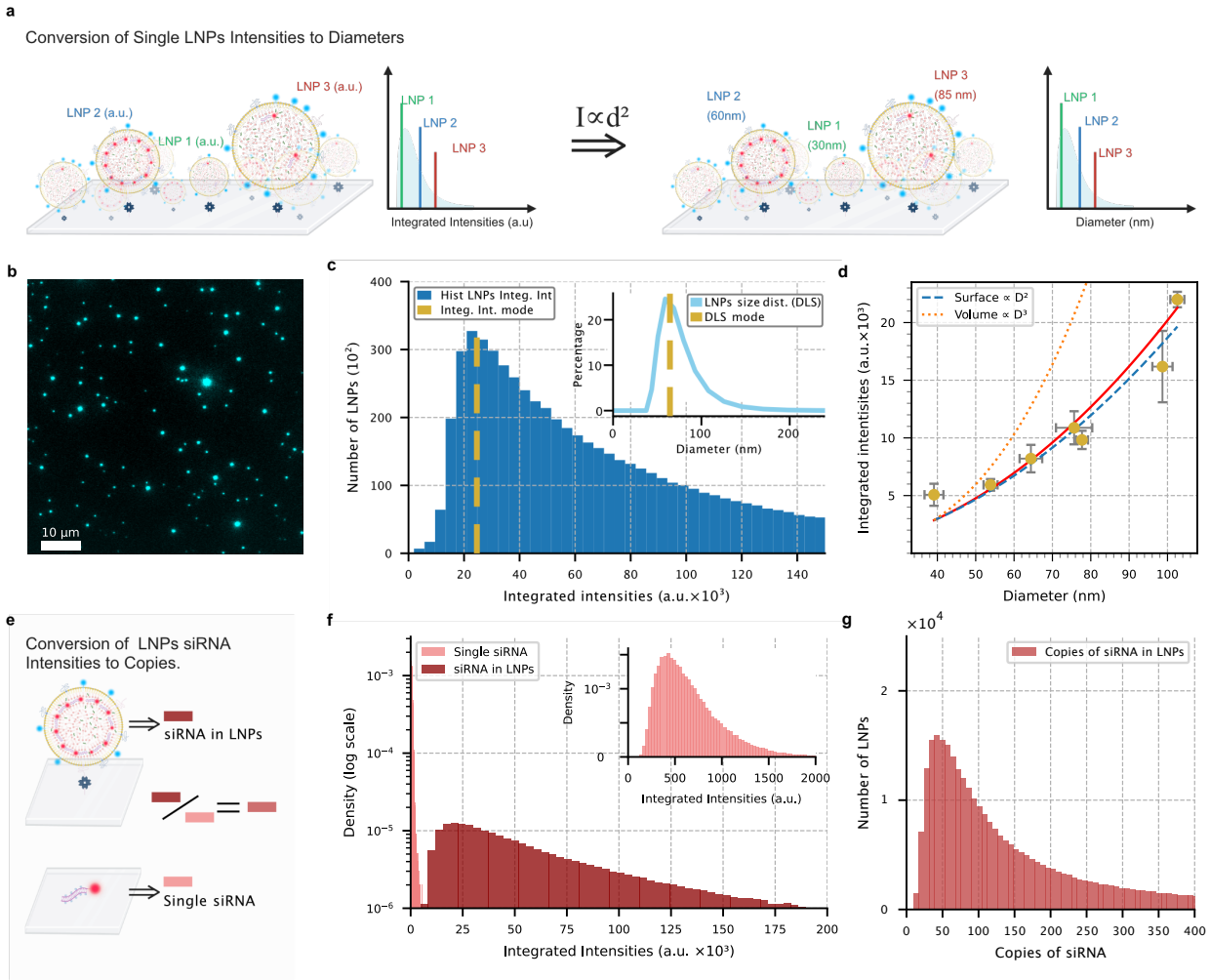

Fig. 1 | Conversion of fluorescence signals into single-LNP size and cargo content. a, *Schematic illustrating the conversion of fluorescence signal from fluorescently labeled lipids into LNP diameter, based on the scaling of fluorescence signal with the square of the particle diameter (d^2).* ***b,*** *Fluorescence micrograph showing individual LNPs tethered on passivated surfaces using streptavidin biotin method. LNPs are below the diffraction limit and appear as point spread functions (PSFs). Notice the large heterogeneity in signal.* ***c,*** *Histogram of background corrected integrated fluorescence intensities from ~10^6 individual LNPs fluorescently labeled with DPPE-ATTO488 (dark blue), with mode intensity indicated (gold). Inset, corresponding size distribution by number from DLS (light blue) with mode size (gold).* ***d,*** *Scaling of the mode of integrated lipid fluorescence intensity for seven LNP populations with identical composition*

and varying diameters, plotted as a function of the mode diameter measured by DLS (error bars St.dev from 3-4 technical replicates). Blue and yellow dotted line correspond to modelled integrated intensity scaling with a cubic or quadratic relationship respectively ***e,*** *Schematic illustrating the conversion of background corrected fluorescence of labeled siRNA to copy number of siRNA encapsulated in each individual LNPs into siRNA.* ***f,*** *Histogram of integrated fluorescence intensities from individual LNPs in the siRNA channel (dark red) and of single labeled siRNA molecules (light red). Inset, zoom-in of the single-siRNA intensity histogram.* ***g,*** *Histogram of measured siRNA copy numbers per LNP, derived from panel f.*

We formulated LNPs containing DPPE-Atto488 as a size-reporting lipid, loaded them with siRNA-AlexaFluor647 and measured their fluorescence intensities using TIRF microscopy (Fig. 1b). Individual particles were immobilized on functionalized glass coverslips via biotin-neutravidin interactions to enable stable single-particle imaging[30,31] (see methods). While each LNP is a diffraction limited spot the integrated intensity of its signal scales will depend on its dimensions with a scaling factor. From these measurements, we extracted the integrated intensity of $>10^5$ LNPs per condition, yielding apparent size distributions in arbitrary units[26–29] (Fig. 1c). Because DLS reports the most frequent physical diameter of the LNPs population, i.e. the mode, and TIRF reports the mode integrated intensity of the same population, the two values can be directly paired, such that the mode TIRF intensity corresponds to the mode DLS diameter, providing a logical reference point to link single-particle fluorescence intensities to physical size (Fig. 1c). However, this correspondence alone is not sufficient to convert individual LNP intensities into diameters; one must also establish how the amount of fluorescently labeled lipid scales with particle size.

To determine this scaling relationship, we generated LNP populations with tunable diameters by varying microfluidic formulation parameters while maintaining a constant lipid composition (Supplementary Table 1). This produced size distributions with mode diameters ranging from ~40 to >100 nm, as measured by DLS (Supplementary Fig. 2). For each population, we measured the integrated DPPE-Atto488 fluorescence and plotted it against the corresponding DLS-derived diameters (Fig. 1c-d). Fitting revealed a quadratic relationship ($I \sim D^2$), consistent with a surface distribution of the DPPE-Atto488 labels (Fig. 1d) as we have shown for. Together, these findings demonstrate that lipid-associated fluorescence provides a quantitative proxy for particle diameter with nanometer-level precision.

We next calibrated the cargo channel to quantify the number of siRNA molecules per LNP. We measured the integrated fluorescence intensity of siRNA-AF647 for individual particles and compared it to the intensity of single surface-immobilized siRNA reference molecules (Fig. 1e). After correcting for differences in exposure time and acquisition settings (Supplementary Fig. 3), the ratio between LNP cargo intensity and single-molecule intensity provided a direct estimate of siRNA copy number. This calibration enabled us to assign absolute RNA cargo counts to each LNP, thereby completing the framework for simultaneous, quantitative measurement of size and cargo at the single-particle level. Together, these results establish a single-particle fluorescence assay that

enables simultaneous measurement of LNP diameter and RNA cargo copy number. The method provides absolute quantification of nanoparticle heterogeneity across $>10^5$ particles per condition (Supplementary Fig. 1) and is broadly compatible with standard fluorescence microscopes.

Quantification of heterogeneity in LNP size and RNA loading

To visualize directly how size heterogeneity alters siRNA loading directly, we first imaged LNPs in both the lipid (top) and siRNA (bottom) channels (Fig. 2a). A zoom-in of a representative region, rendered as a 3D surface plot, highlights striking particle-to-particle differences in cargo content relative to size (Fig. 2b-c). Four example LNPs illustrate this variability: particles 1 and 2 exhibit comparable lipid intensities, consistent with similar diameters, yet particle 2 contains vastly more siRNA than particle 1. Conversely, particle 3 is larger than particle 1 based on lipid signal but carries fewer siRNA molecules. These examples, quantified in a schematic (Fig. 2c), showcase that LNP size does not deterministically predict RNA cargo loading.

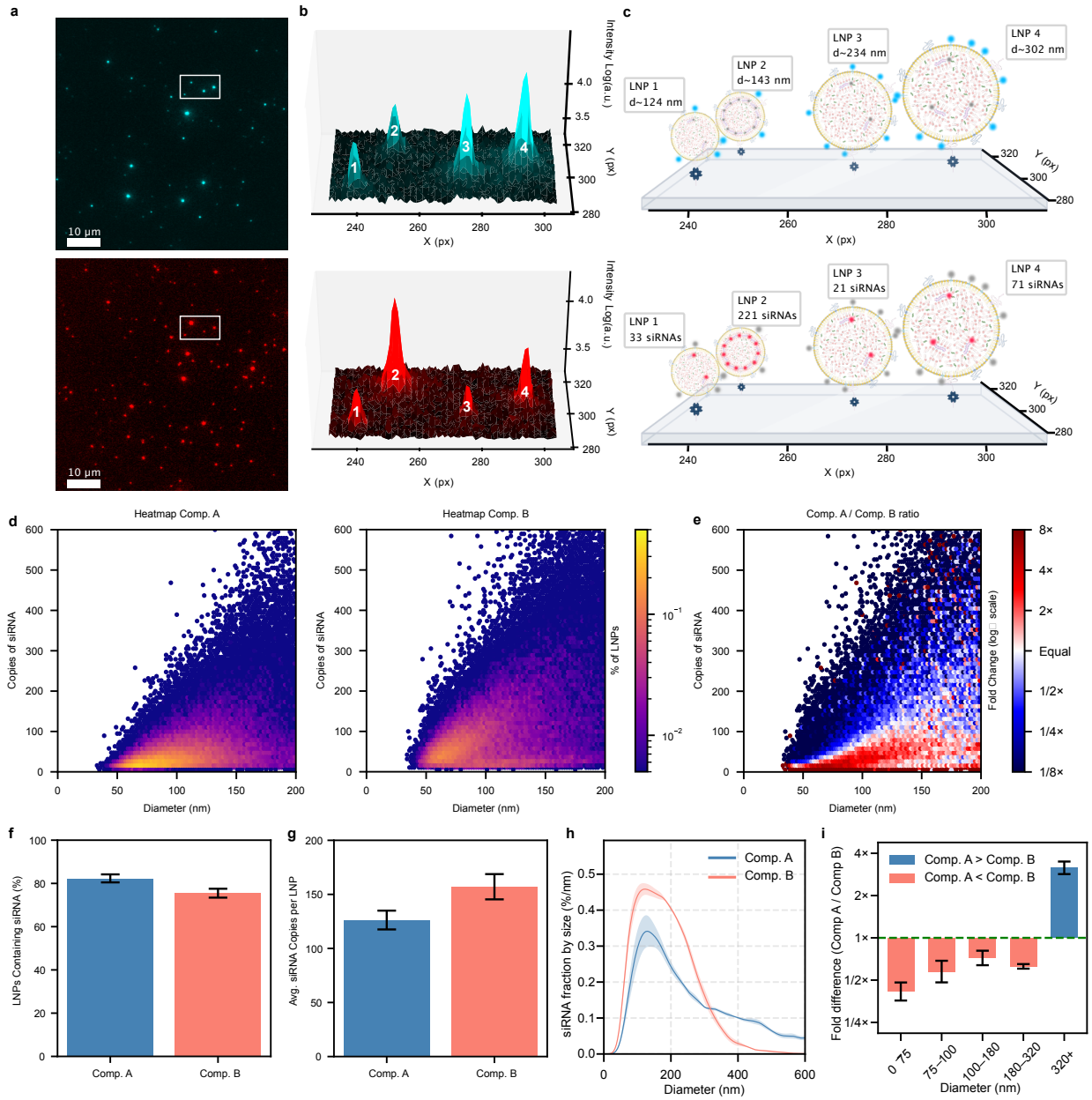

Fig. 2 | Quantification of single LNP heterogeneity in size and siRNA loading for two lipid formulations. a, *Fluorescence TIRF micrographs of individual LNPs in the lipid (top) and siRNA (bottom) channels.* ***b,*** *3D surface plots of fluorescence intensity within the white rectangle in* a*, showing LNPs in the lipid (top) and siRNA (bottom) channels. LNPs are heterogenous in dimensions and in siRNA loading.* ***c,*** *Schematic of the four LNPs shown in* b*, annotated with their estimated diameters (top) and siRNA copy numbers (bottom). Notice, the particle-to-particle heterogeneity in cargo content relative to LNP size.* ***d,*** *Heatmaps of siRNA copy number as a function of LNP diameter for lipid composition A (left) and composition B (right), based on >100,000 single LNPs per condition. Data granularity reveals that lipid composition affects loading* ***e,*** *Ratio metric heatmap showing the fold difference in LNP density between compositions A and B across the diameter-cargo space.* ***f,*** *Bar plot showing the percentage of LNPs containing siRNA for each composition, calculated over the entire population.* ***g,*** *Bar plot showing the average number of siRNA copies per LNP for each composition.* ***h,*** *Kernel-density-based distribution of total siRNA content as a function of LNP diameter for composition A and B, shown as mean ± St. dev.* ***i,*** *Fold difference in the percentage of siRNA copies across five defined size bins: 0-75 nm, 75-100 nm, 100-180 nm, 180-320nm and >300 nm. All data correspond to 3-4 technical replicates and error bars correspond to St.dev. of the 3-4 technical replicates.*

We next scaled this analysis to entire populations of two representative and well-established formulations differing in ionizable lipid content and composition, Comp A and Comp B (see methods). Heatmap scatter plots of siRNA copy number versus particle diameter revealed distinct loading landscapes (Fig. 2d). Although both formulations exhibited similar size distributions (Supplementary Table 2), their cargo organization differed: Comp B showed a broader dispersion of siRNA copy numbers across sizes, whereas Comp A was modestly enriched in higher siRNA content across much of the diameter range. Ratiometric comparison (Fig. 2e) highlighted distinct regions of enrichment, with Comp B strongly biased toward higher cargo content across a broad size range, while Comp A contributed more to the low-loaded small-particle regime.

Despite these differences at the single-particle level, bulk-like summary statistics painted a deceptively similar picture. Both formulations contained a comparable percentage of RNA-loaded particles (Fig. 2f) and siRNA copy numbers (Fig. 2g). Because such ensemble averages obscure how siRNA cargo is distributed across the nanoparticle size spectrum we quantified the distribution of total siRNA content as a continuous function of LNP size spectrum (Fig. 2h). Both LNPs concentrate most of their siRNA within the intermediate diameter range, with broadly similar maxima. Interestingly while Comp B distributes siRNA broadly across mid-sized particles, Comp A progressively shifts a substantial fraction of its total siRNA into the largest particles, creating a pronounced high-diameter bias absent in Comp B. Stratifying total siRNA content into five diameter intervals revealed a consistent depletion of Comp A as compared to Comp B at smaller and mid-sized particles (0.42X at 0–75 nm; 0.58X at 75–100 nm; 0.72X at 100–180 nm; 0.63X at 180–320 nm), with inversion only in the largest bin (>320 nm; 3.15X) (Fig. 2i). Thus, despite similar mean loading, the formulations diverged sharply in cargo allocation, with Comp A enriching its largest nanoparticles. Thus, while both formulations encapsulated RNA efficiently overall, they distributed it differently across the nanoparticle size range. While bulk dosing based on input RNA concentration captures differences in mean loading, it fails to resolve this size-dependent cargo partitioning. Single-particle analysis instead reveals distinct loading landscapes reframing particle-to-particle heterogeneity from a confounding feature of ensemble assays into a measurable variable.

Single-particle analysis reveals diverse packing states underlying LNP cargo heterogeneity

To uncover the structural basis of these heterogeneous loading distributions, we generated and analyzed in Fig. 3 the joint size-cargo kernel density estimate (KDE) contour plot at single-particle resolution of the data in Fig 2a. Even visual inspection of these density landscape revealed two preferential modes of siRNA loading, a low-density band and a higher-density branch that diverged progressively with particle size, suggesting a hidden binary-like organization of RNA packing within an otherwise uniform LNP formulation (Fig. 3a). Control experiments with mixed labeled and unlabeled siRNA confirmed that the observed bimodality is not driven from fluorophore quenching (Supplementary Fig. 4).

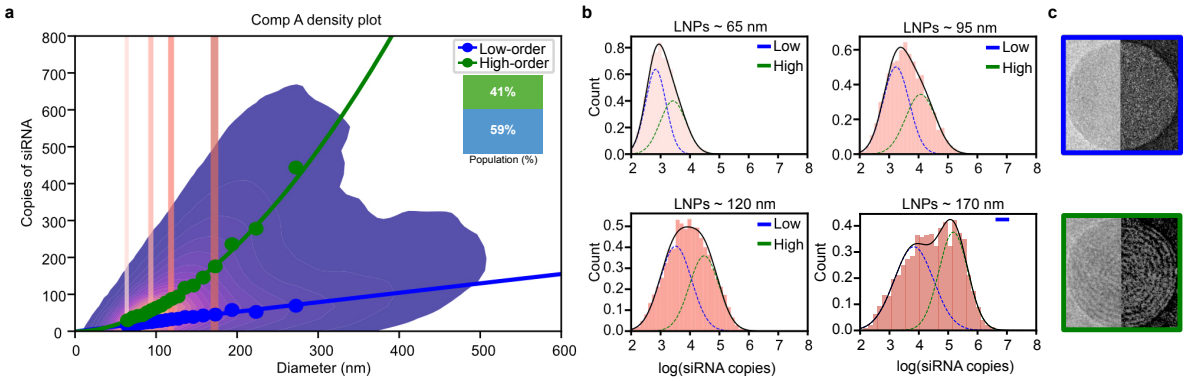

Fig. 3 | Heterogeneity in siRNA loading LNPs reveals distinct subpopulations with different scaling behaviors. *Two-dimensional kernel density estimate (KDE) contour plot of siRNA copy number versus LNP diameter for formulation A reveals two distinct populations with different power-law scaling behaviors. Power-law fits are overlaid for the high-order (exponent: 1.92 ±0.08) and low-order (exponent: 1.05 ± 0.08) populations, averaged across four technical replicates. Inset indicates the relative abundance of each population (41±3% high-order and 59±3% low-order; n = 4 technical replicates).* ***b,*** *Log-transformed histograms of siRNA copy number for LNPs within four diameter percentile bins (55 nm, 85 nm, 115 nm, and 165 nm), corresponding to the 5th, 30th, 50th, and 75th percentiles, as indicated by color-matched tick marks in a. Two-component Gaussian mixture models reveal bimodal distributions corresponding to low- (blue) and high-order (green) loading states*

To quantify this apparent bifurcation, we divided the size-cargo map of Comp A into percentile-centered diameter bins and modeled the log-transformed siRNA distribution within each bin (Fig. 3a). The Bayesian Information Criterion (BIC) was used as a quantitative proxy for model likelihood under a Gaussian assumption, to evaluate multimodality in siRNA loading distributions (Supplementary Fig. 5). Across most conditions, the BIC favored a two-component Gaussian model over a single one, supporting low-load and high-load particle populations with diverse internal packing densities. Log-histograms from representative size bands confirmed the bimodal siRNA distributions, with greater separation at larger diameters (Fig. 3b). Cryo-electron microscopy revealed two general types of electron densities, a low density, low order like morphology corresponding to electron-lucent amorphous and bleb-like particles and a higher density, higher packing order morphology, corresponding to multilamellar and locally inverse-hexagonal particles (Fig. 3c, Supplementary Fig. 6). This observation is consistent with the two populations identified by mixture modeling, and earlier reports showcasing multiple packing of LNPs [12,15–17]. It also verifies the differential packing modes are not artifacts of differential chromophore quenching. Across the population, the 2-component mixture model estimated that approximately 59±3% of particles belong to the low-order state and 41±3% to the high-order state (Fig. 3a), indicating that both architectures coexist in comparable proportions.

Plotting the component means in log-log space uncovered two separate scaling laws of siRNA content with diameter (Supplementary Fig. 7). Linear fits in this transformed space yielded slopes of 1.05 ± 0.08 for the low-order and 1.92 ± 0.08 for the high-order populations. In Fig. 3a, the corresponding power-law relationships are shown as blue and

green lines overlaid on the linear-scale kernel density map, where their separation becomes visually evident. The weaker scaling of the low-order state is consistent with amorphous or disordered internal organization, whereas the near-quadratic dependence of the high-order state suggests multilamellar and locally inverse-hexagonal shell architectures, consistent with our and others Cryo-EM (Supplementary Fig. 7)[12,14,15,17,18,32]. A single global fit collapsed these trends, supporting that LNP heterogeneity arises from discrete structural subpopulations rather than stochastic variation. Stochastic coagulation simulations of LNP self-assembly reproduced comparable sub-volumetric exponents (Methods; Supplementary Fig. 8), supporting that the observed scaling naturally arises from probabilistic merger dynamics rather than surface-limited loading, consistent with earlier reports [33–35]. Thus, the experimentally observed scaling exponents reflect intrinsic constraints of the assembly process, while the coexistence of two distinct scaling regimes points to additional structural organization beyond stochastic variability. What appears as stochastic heterogeneity at the population level instead reflects two major self-assembled organizational states with distinct physical scaling and functional potential.

Lipid composition tunes mesoscale packing and functional delivery

To test whether lipid composition modulates RNA packing architecture, we used the two well established composition Comp A and Comp B (See Methods, Supplementary Table 2). KDE plots of siRNA copy number versus LNP diameter for ~0.5 million particles per formulations revealed marked shifts in packing-state distribution (Fig. 4a,b), corroborated by cryo-EM micrographs showing LNPs with predominantly amorphous interiors in Comp A and multilamellar architectures in B (Supplementary Fig. 6). Comp A (N/P 3) contained 59 ± 3% low-order particles with a mean scaling exponent of 1.05 ± 0.08 (Fig. 4a), whereas Comp B (N/P 3) contained only 32 ± 1% low-order particles with a shallower exponent of 0.70 ± 0.12 (Fig. 4b). High-order scaled with exponents of 1.92 ± 0.08 (Comp A) and 1.30 ± 0.04 (Comp B), respectively, with these differences reproducible across 4 technical replicates (See Supplementary Fig. 9 for individual replicates). Lipid composition thus reproducibly governs nanoscale packing order.

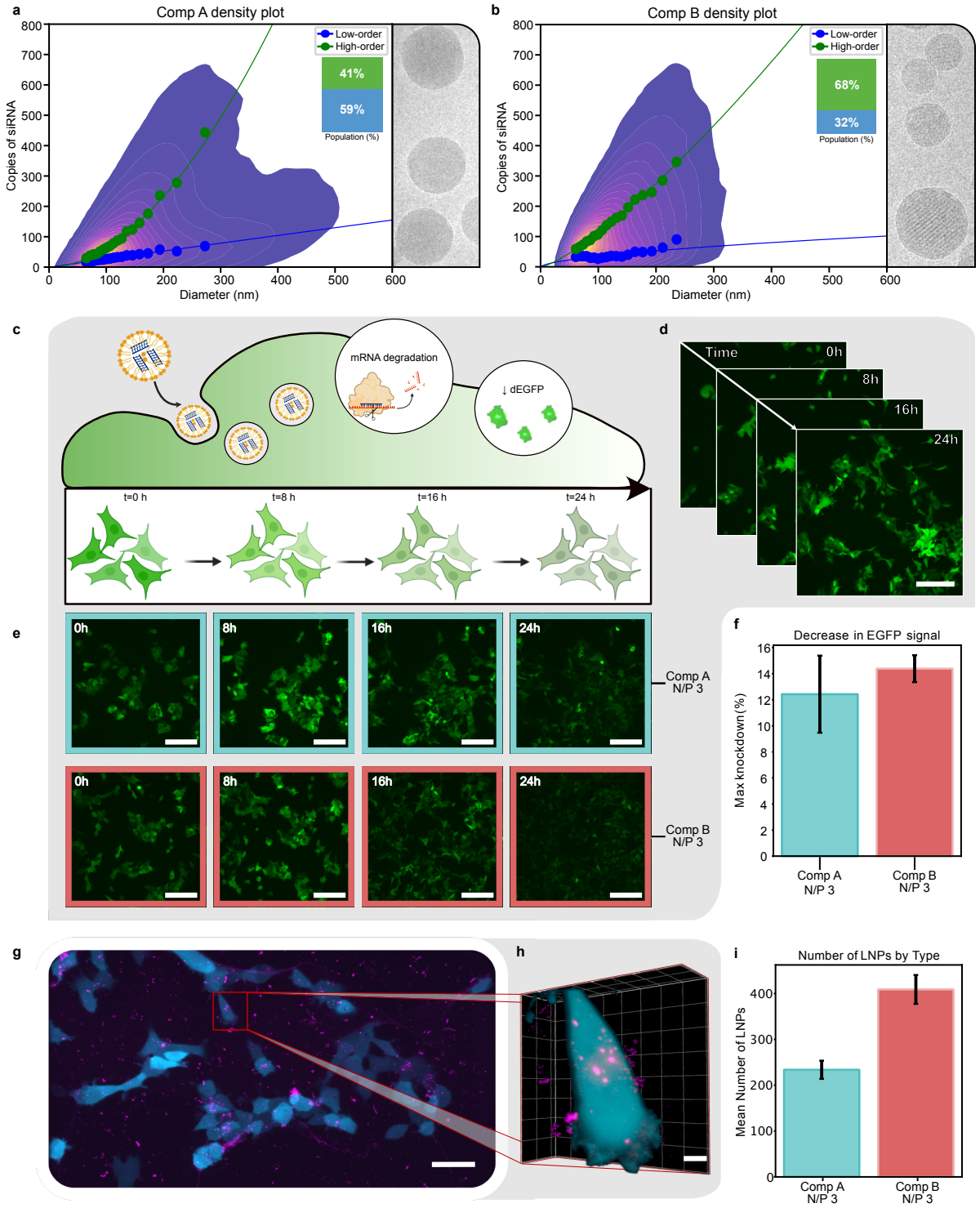

Fig. 4 | LNP composition modulates siRNA loading order influencing siRNA mediated target knockdown. a, b, *Two-dimensional KDE contour plots of siRNA copy number versus LNP diameter for formulations A and B (left). KDE contour plots are representative of four independent technical replicates. Insets quantify the relative abundance of low- and high-order packing states, averaged across the four technical replicates. Representative cryo-electron microscopy images displaying mostly amorphous packing in A and mostly concentric architecture in B consistent with diverse packing of KDEs.* ***c,*** *Schematic illustration of experimental setup of cellular uptake of LNPs, siRNA release, and*

subsequent eGFP knockdown. ***d,*** *Representative spinning-disk confocal time series of untreated HEK293T-d2eGFP cells (Scale bar, 50 µm).* ***e,*** *Representative spinning-disk confocal images of HEK293T cells expressing d2eGFP at 0 h, 8 h, 16 h, and 24 h following treatment with siRNA-loaded LNPs (300 nM). Images show the progressive decrease in eGFP fluorescence over the assay. For visualization, the z-plane with maximal eGFP fluorescence was selected, and display settings were kept constant across conditions (Scale bar, 50 µm).* ***f,*** *Quantification of d2eGFP knockdown after 24 h, showing reduced fluorescence intensity relative to untreated controls. Bars show mean ± S.E.M. from three independent technical replicates. Statistical significance was assessed using Welch's t-test (P = 0.586; ns).* ***g,*** *Maximum-intensity projection of a lattice light-sheet microscopy (LLSM) dataset showing LNP internalization into d2eGFP-HEK293T cells (Scale bar, 50 µm).* ***h,*** *Representative 3D LLSM reconstruction of a single cell with internalized LNPs (Scale bar, 5 µm).* ***i,*** *Quantification of internalized LNPs per cell for formulations A and B. Bars show mean ± S.E.M. from three independent biological replicates. Statistical significance was assessed using Welch's t-test (P = 0.014; *).*

We next examined whether the compositional control of nanoscale packing order manifests in differences in uptake and functional siRNA delivery. We added Comp A and Comp B of siRNA loaded LNPs (300 nM; Supplementary Table 3; Fig. 4c) to HEK293T cells stably expressing destabilized eGFP (d2eGFP) (see Methods). Live cell imaging[36,37] using time-lapse spinning-disk microscopy revealed progressive loss of fluorescence over 24 h following treatment with siRNA-loaded LNPs (Fig. 4d,e; Supplementary Fig. 10). Quantification across three independent technical replicates confirmed comparable knockdown efficiencies of 12 ± 3 % for Comp A and 14 ± 1 % for B relative to untreated controls (Fig. 4f, Supplementary Fig. 11). Interestingly however Lattice light sheet and quantitative image analysis revealed cells internalized ~1.7 times more LNPs of Comp A than Comp B after 2.5h of incubation (Fig. 4g,h; Methods; Supplementary Fig. 12): an average of 234 ± 20 particles for Comp A and 409 ± 31 for B, (Fig. 4i). Notably both formulations had comparable hydrodynamic diameters (~80 nm; Supplementary Table 3 and Fig. 13), indicating that lipid chemistry rather than particle size governs internalization efficiency[38].

To disentangle how entry, release, and structure jointly shape delivery outcomes, we compared the relative abundance of entering particles and amorphous fractions across formulations. Comp B internalized ~1.7-fold more LNPs per cell than Comp A, yet Comp A contained ~1.7-fold more low-order, amorphous particles. These mirrored ratios suggest that the higher uptake of B is counterbalanced by the greater fraction of potentially release-competent particles in A, resulting in similar overall knockdown efficiencies. Mesoscale packing differences[39,40], appears to modulate the balance between uptake and cytosolic release rather than the total amount of internalized RNA. To assess whether packing order itself predicts release efficiency independent of lipid composition, we next modulated LNP self-assembly by varying the N/P ratio.

Low-order, amorphous LNPs outperform ordered architectures in siRNA delivery

To isolate the effect of packing order from lipid composition, we systematically varied the N/P ratio while keeping formulation chemistry and microfluidic parameters constant. KDE plots of siRNA copy number versus LNP diameter revealed a pronounced dependence of packing organization on N/P ratio (Fig. 5a-c). LNPs formed at N/P 1 were exclusively high-order, whereas N/P3 and 6 yielded mixed populations with progressively higher low-order

fractions of 59 ± 3% and 61 ± 2%, respectively, consistent with qualitative readout of Cryo-EM measurements (Supplementary Fig. 6). Across conditions, both packing modes exhibited sub-volumetric scaling, but with condition-specific exponents: at N/P 3, the low-order and high-order branches were 1.05 ± 0.08 and 1.92±0.08, respectively; at N/P 6, they shifted to b = 0.85 ± 0.10 (low-order) and 1.43 ± 0.17 (high-order). N/P 1 displayed only the high-order branch (1.81 ± 0.07). These values indicate that N/P tuning alters both the relative abundance and, to a lesser extent, the effective scaling of each packing mode**.** Percentile-matched histograms centered at ~150nm confirmed unimodal intensity distribution at N/P 1 and bimodal low-/high-order mixtures at N/P 3 and 6 (Fig. 5d-f). There structural differences were reproducible across replicates (Supplementary Fig. 5,14,15), demonstrating that electrostatic stoichiometry at the point of complexation directly governs nanoscale RNA packing.

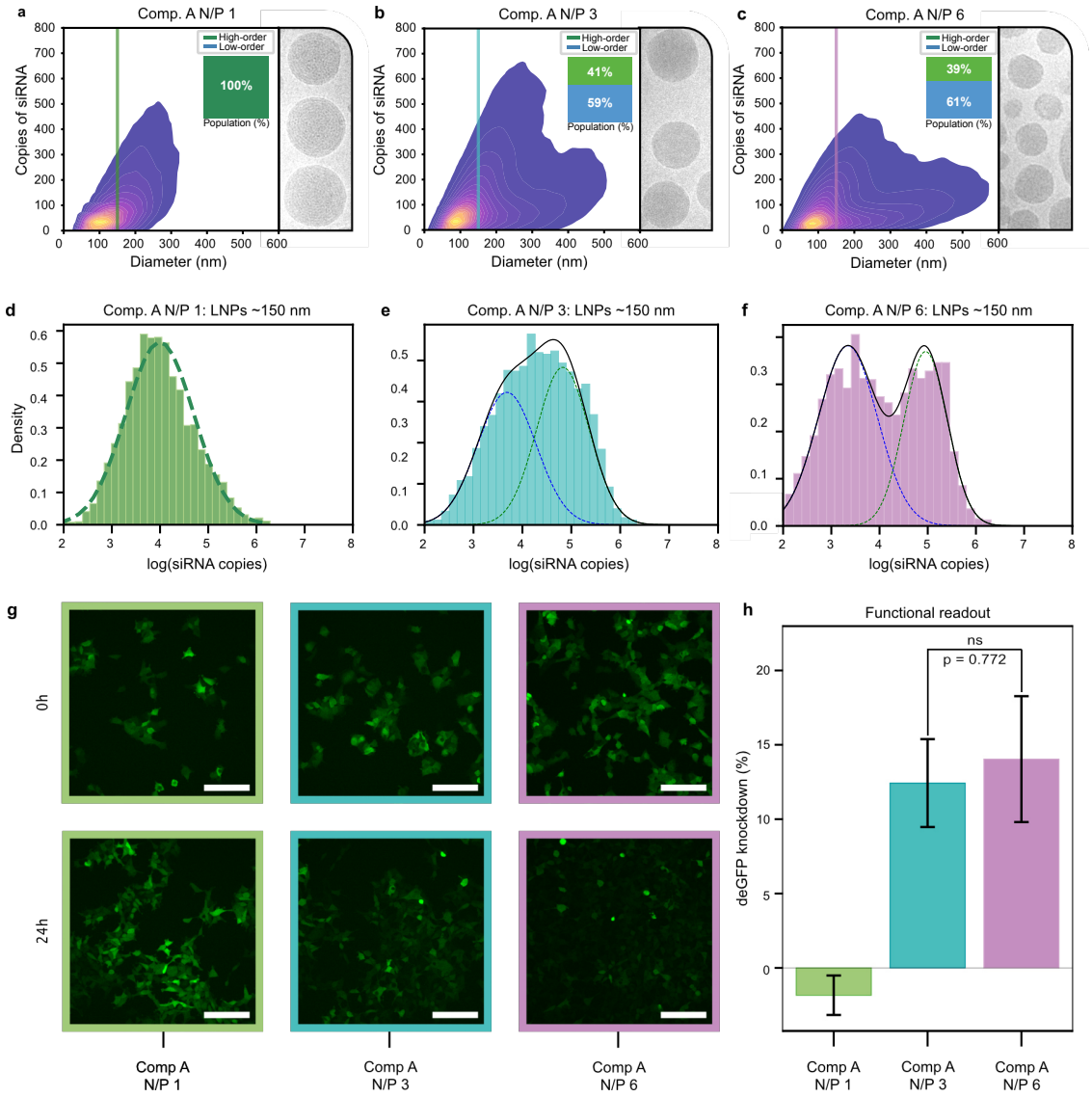

Fig. 5 | Low-order siRNA packing states correlate with enhanced siRNA-mediated knockdown activity a-c, *Effect N/P ratios to packing order. Two-dimensional KDE contour plots of siRNA copy number versus LNP diameter for formulation A at N/P ratios of 1, 3, and 6). KDE contour plots are representative of four independent technical replicates. Insets quantify the relative abundance of low- and high-order packing states, averaged across the four technical replicates. N/P 1 yields exclusively high-order particles, while N/P 3 and 6 show mixed populations. KDEs are consistent with representative cryo-electron microscopy images:* ***d-f,*** *Log-transformed histograms of siRNA copy number for LNPs within percentile bins centered around 150 nm, as indicated in a-c. Gaussian mixture modeling reveals unimodal distributions at N/P 1 (high-order only) and bimodal distributions at N/P 3 and 6, corresponding to low-order (blue) and high-order (green) subpopulations.* ***g,*** *Representative spinning-disk confocal images of HEK293-d2eGFP cells at the first and last time point of the 24 h knockdown assay (see Methods). Images illustrate the initial eGFP fluorescence level and its decrease following treatment. For visualization, the z-plane with maximal eGFP fluorescence was selected, and display settings were kept constant across all conditions (Scale bar, 50 μm).* ***h,*** *Quantification of d2eGFP knockdown in HEK293T cells after 24 h of treatment with siRNA-loaded LNPs (300 nM). Only formulations containing low-order subpopulations (N/P 3 and 6) induce knockdown. Purely high-order particles (N/P 1) display no measurable knockdown. Bars represent mean ± S.E.M. from three independent technical replicates. Statistical significance was assessed using Welch's t-test; no significant difference was observed between N/P 3 and N/P 6 (P = 0.772; ns).*

We next evaluated how these structural states influence functional delivery. Time-lapse spinning-disk microscopy of HEK293T cells stably expressing eGFP revealed progressive fluorescence decrease over 24 h following treatment with siRNA-loaded LNPs (300 nM; Supplementary Table 3; Fig. 5g; Supplementary Fig. 10). Quantification across three technical replicates showed measurable knockdown for formulations containing mixed populations (N/P 3 and 6), reaching 12 ± 3% and 14 ± 4% reduction, respectively, relative to untreated controls (Fig. 5h). These values were statistically indistinguishable ($p = 0.772$), indicating comparable functional efficiency between N/P 3 and N/P 6. The low-order fractions at N/P 3 and N/P 6 were statistically indistinguishable (59 ± 3% vs 61 ± 2%, $p = 0.33$), indicating that both formulations populate a similar mixed-order regime. In contrast, N/P 1, which lacked detectable low-order particles, produced no measurable knockdown, establishing that the presence of low-order architectures is essential for productive release, whereas purely high-order particles are functionally inert.

Together, these findings demonstrate that RNA-packing order, rather than lipid composition alone, governs the efficiency of siRNA endosomal escape and cytosolic delivery. Low-order architectures appear more conductive to functional release, whereas highly ordered, multilamellar states or inverse hexagonal are less efficient in supporting productive delivery. Electrostatic control of complexation thus provides a runnable handle to modulate LNP organization, revealing that low-order amorphous architectures enhance functional RNA release and functional potency.

Discussion

This study bridges a long-standing mechanistic gap between LNP architecture and functional delivery by linking single particle loading heterogeneity with nanoscale packing order and cytosolic release efficiency. Hight throughput imaging across ~0.5 million

single-particle measurements per condition, uncovered two siRNA packing modes, low-order, amorphous, and high-order, multilamellar, whose relative abundance can be tuned by lipid composition and electrostatic stoichiometry. Counterintuitively, while high-order particles encapsulate larger amounts of siRNA, low-order structures exhibit markedly greater delivery efficiency, as evidenced by their enhanced knockdown of a destabilized GFP reporter. These results reveal that electrostatic complexation not only dictates encapsulation efficiency but also programs the internal order of the assembled nanoparticle, which in turn modulates functional outcome.

Mechanistically, our data could suggest that low-order particles representing more deformable, metastable assemblies whose internal disorder facilitates efficient cargo release. Amorphous organization may promote local curvature fluctuations and expose ionizable lipid headgroups upon acidification, lowering the energetic barrier for fusion or transient pore formation. This structure could also result in less dense packing of siRNA that is more efficiently released upon endosome rupture[41] than their high ordered counterparts. By contrast LNPs with stacked, highly ordered bilayers, could likely resist curvature stress and may hinder water and ion penetration, impeding the structural rearrangements required for release. This interpretation aligns with reports on specialized LNP compositions showing less ordered and hexagonal phases are corelated to improved knockdown efficiency[12,17,18].Similar principles govern viral uncoating, where productive delivery requires a finely tuned balance between stability during trafficking and susceptibility to triggered disassembly[42]. Moreover, recent imaging studies show that classical rupture markers such as galectin recruitment[9], do not necessarily predict productive release, despite endosomes remain perforated for periods of time[43]. In this view, low-order packing may represent an energetically “primed” configuration that preserves integrity extracellularly but remains responsive to endosomal acidification, enabling efficient cytosolic access. High order on the other hand may maintain its stability in ruptured endosomes thereby preventing efficient functional release.

While our findings reveal a direct link between nanoscale packing and delivery efficiency, several questions remain. The causal molecular events that underlie release and their dependence on the described packing modes, remains elusive. Extending current experiments from model cell line to primary cells and in vivo settings will be critical to determine whether the same structure, function relationships persist in additional cellular environments. Evaluation of the potential existence of diverse packing modes on mRNA or ASOs may offer crucial insights for enhancing their delivery. ASOs siRNA and mRNA differ significantly in rigidity, length, and charge distribution, likely favoring distinct internal organizations. The single particle platform here can decipher potential correlations between structural organization and release efficiencies thereby tailoring functional mRNA delivery. Future work combining our single-particle readouts with live-cell endosomal tracking could directly visualize release events, quantify their dependence on

packing and, ultimately, established a universal mechanistic link between nucleic therapeutic organization and cytosolic entry.

Previous studies have correlated composition and N/P ratio with organization into lamellar, hexagonal, or inverted micellar arrangements[10,11,15,17] but lacked direct evidence connecting internal organization to biological performance. The observed transitions from multilamellar to amorphous interiors as N/P increased by Mo, Y. et al, was correlated to LNP responsiveness to external stimuli and light activated siRNA endosomal escape[17]. Similarly, ensemble measurements of phase behavior or pH-triggered transitions[16,18] capture population averages that obscure the coexistence of distinct structural subpopulations. Our single-particle framework extends these insights by showing that these structural modes are not continuum states but, reproducible organizations whose abundance can be modulated. Mesoscale packing order thus may act as a key determinant of LNP efficacy, that is tunable to enhance functional release.

The observed correlation between N/P-dependent packing and delivery performance also highlights how electrostatics shape performance. Higher N/P ratios may increase the charge density at the point of complexation, promoting charge neutralization and condensation, favoring consequently more compact order. Conversely, near-stoichiometric conditions at lower N/P ratios yield more disordered assemblies, probably with increased water content and local defects. Our findings suggest that the most effective formulations need to strike an intermediate regime, sufficiently compact to efficiently encapsulate cargo but disordered enough to enable disassembly and functionality. This electrostatic–structural interplay provides a key predictive framework for rational design of LNPs tuned for loading and biological activity.

The high throughout single LNP readout here combined with quantitative live cell image analysis transform internal LNP architecture from an observational property into a controllable parameter, and to actionable design rules: favoring less compact packing enhances cytosolic bioavailability and silencing potency. The platform introduced here provides a quantitative foundation for rational optimization and is poised to guide the next generation of engineered RNA therapeutics.

Acknowledgements

Work was funded by the Novo Nordisk foundation challenge center for Optimised Oligo escape (NNF23OC0081287), the center for 4D cellular dynamics (NNF22OC0075851) VILLUM FONDEN (40516 and 40801), and Lundbeck foundation Nanopans Project (R453-2024-359**).** N.S.H. is affiliated with The Novo Nordisk Foundation Center for Protein Research funded by a generous donation from the Novo Nordisk Foundation (grant no. NNF14CC0001). N.S.H. is member of the Integrative Structural Biology Cluster at the University of Copenhagen.

Author Contribution

AB, GK and NSH wrote the paper with feedback from all authors. GK and AB performed LNP formulation and characterization. GK performed spinning disk cell imaging with assistance from GB and FHS performed Lattice light sheet cell imaging with the help of AB and GK. GK, and FHS, handled cell culturing and plating with the help of GB and VP. GB generated HEK293T stably expressing d2eGFP with the help of VP. GK performed the cryo-EM experiments with the help of AB. AB developed the analysis algorithms and pipelines with help from GK. AB analyzed the data with the help of GK. MD prepared the lipid packing model and developed the analysis code with inputs from AB and GK. SM and NS performed preliminary experiments and analysis. NSH conceived the project, acquired funding and had the overall supervision and project management.

Disclaimer

N.S.H. is the CSO and co-founder of EDGE Biotechnologies. A.B. is part time employee of EDGE Biotechnologies.

Methods

Materials

1,2-distearoyl-sn-glycero-3-phosphocholine (DSPC, 850365P), 1,2-dioleoyl-sn-glycero-3-phosphoethanolamine-N-[methoxy(polyethylene glycol)-2000] (ammonium salt) (PEG2000-PE, 880130P), and 1,2-distearoyl-sn-glycero-3-phosphoethanolamine-N-[biotinyl(polyethylene glycol)-2000] (ammonium salt) (PEG2000-DSPE-biotin, 880129P) were purchased from Avanti Polar Lipids (Alabaster, AL, USA). Cholesterol (C8667) was obtained from Sigma-Aldrich (St. Louis, MO, USA). 9-Heptadecanyl 8-{(2-hydroxyethyl)[6-oxo-6-(undecyloxy)hexyl]amino}octanoate (SM-102, HY-134541), ([(4-hydroxybutyl)azanediyl]di(hexane-6,1-diyl) bis(2-hexyldecanoate)) (ALC-0315, HY-138170), and 2-[(polyethylene glycol)-2000]-N,N-ditetradecylacetamide (ALC-0159, HY-138300) were obtained from MedChemExpress LLC (Monmouth Junction, NJ, USA). DPPE-ATTO488 (AD 488-151) and DPPE-ATTO655 (AD 655-151) were acquired from ATTO-TEC GmbH (Siegen, Germany). eGFP-targeting siRNA with Alexa Fluor 647 conjugated at the 3′ end of the sense strand (eGFPsiRNA_sense3′Alexa647N) was purchased from Integrated DNA Technologies (IDT, Coralville, IA, USA). Silencer™ eGFP siRNA (AM4626) was obtained from Invitrogen (Thermo Fisher Scientific, Waltham, MA, USA).

LNP formulation and characterization

Microfluidics: LNP formulation

Ethanol solutions of the lipid mixes at indicated molar ration and total lipid concentration were prepared, as described in Supplementary Tables 1-3. The RNA was diluted in 10mM citrate buffer pH 4 (132-04-3, Thermo Fisher Scientific, Waltham, MA, USA). LNPs were prepared using a staggered herringbone micromixer (SHM) glass chip, with channel depth of 0.08mm (LTF-012.00-4264, Darwing Microfluidis, Paris, France) as the microfluidic device. The lipid mixture and the RNA solution were injected into the SHM via 250 µL PTFE Peek Syringes (10103660, Hamilton, Reno, NV, USA) and mixed at a N/P ratio of 3.

The SHM features three converging inlets, where the organic phase containing the lipid mixture flows through the two outer channels and the central channel delivers the aqueous phase comprising RNA. Flow rates were control by a Pump 33 dual drive system (703333, Harvard Apparatus, Massachusetts, USA). LNPs were collected at the outlet in 1.5 mL of 1X PBS PH 7.4 (AM9625, Invitrogen, Thermo Fisher Scientific, Waltham, MA, USA), to bring ethanol concentration below 5%. Residual ethanol was removed by overnight dialysis at 4 °C in 1X PBS using 100kDa molecular weight cut-off (MWCO) dialysis tubing (131420, Biotech, Repligen, USA). The LNP suspensions were concentrated by centrifugation at 4000 × g for 30 min at 4 °C using 10 kDa MWCO Amicon Ultra-4 centrifugal filter units (UFC8010, Merck Millipore, Burlington, MA, USA).

Encapsulated RNA was quantified using a modified Quant-iT™ RiboGreen™ RNA Assay (R11490, Invitrogen, Thermo Fisher Scientific, Waltham, MA, USA). A Triton-based calibration curve (1× TE + 0.5% Triton X-100) was generated using the same siRNA as in the LNP formulations (Silencer™ eGFP siRNA). Each sample was measured in parallel as free RNA (1× TE) and total RNA (1× TE + 0.5% Triton X-100). After incubation with RiboGreen working reagent, fluorescence was blank-corrected and converted to RNA concentration. Encapsulated RNA was determined as total minus free RNA, corresponding to the RNA protected within intact LNPs.

Dynamic light scattering: Size characterization of LNPs

The hydrodynamic diameter of lipid nanoparticles (LNPs) was measured by dynamic light scattering (DLS) using a Zetasizer Pro system (Malvern Panalytical, UK). Samples were diluted in 1X PBS to achieve comparable particle concentrations across formulations. For each LNP formulation, three independent technical replicates were prepared. Each

replicate was measured three times consecutively, and the resulting values were averaged. The overall mean particle size and standard deviation were then calculated from the set of technical replicate averages.

Cryogenic Transmission Electron Microscopy

Lipid nanoparticles (LNPs) were concentrated to a final total lipid concentration of ~15 mg/mL. Lacey carbon 300 mesh copper grid (Ted Pella Inc., Redding, CA, USA) was glow discharged on Ace 200 Leica glow discharge unite (30 sec at 15mA). A 3µL aliquot of the suspension was applied to the grid and plunge-frozen using a Mark IV Vitrobot (FEI, Hillsboro, OR), with a blot-force of 4 for 3 seconds to generate vitreous ice. Grids were stored in liquid nitrogen prior to imaging. Cryogenic transmission electron microscopy (cryo-TEM) was performed using a Tecnai G2 20 microscope (Thermo Fisher Scientific, USA) operated at 200 kV under low-dose rate. Images were acquired with a bottom mounted FEI High-Sensitive (HS) 4k × 4k Eagle camera. All sample preparation and imaging were carried out at the Core Facility for Integrated Microscopy, University of Copenhagen (Copenhagen, Denmark).

Total Internal Reflection Fluorescence microscopy: Single-particle fluorescence assays

Single-particle experiments were conducted using an inverted total internal reflection fluorescence (TIRF) microscope, model IX83 (Olympus). The system was equipped with an electron-multiplying charge-coupled device (EMCCD) camera (ImagEM X2, Hamamatsu), a 100× oil immersion objective lens (UAPON 100XOTIRF, NA 1.49, Olympus) and a quad-band emission filter cube designed to remove excitation laser light from the detection pathway. Fluorescence excitation was achieved using two solid-state lasers (Olympus) operating at wavelengths of 488 nm (Atto488-labeled lipids) and 640 nm (Alexa647-labeled cargo). Prior to acquisition, optimal focus and TIRF angle were established. Data were acquired with a 200nm evanescent field penetration depth, an EM gain setting of 300, and image resolution of 512 × 512 pixels in 16-bit grayscale. Each acquired field of view corresponds to a physical area of 81.92 μm^2.

TIRF: High-throughput single-particle characterization of LNPs

Plasma activated glass slides (80608, Ibidi, Martinsried, Germany) incorporating sticky-Slide VI 0.4 (10812, Ibidi, Martinsried, Germany) were functionalized using PLL-g-PEG and PLL-g-PEG-biotin (Susos AG, Dübendorf, Switzerland) at a 100:1 ratio. A neutravidin

(11544037, Fisher Scientific, Waltham, MA, USA) layer was subsequently applied to enable specific immobilization of biotinylated particles.

Biotinylated LNPs diluted in 1X PBS buffer pH 7.4 were injected into the microfluidic channel and incubated for 10 min to allow surface immobilization. The concentration was adjusted to achieve densities of approximately 40-70 LNPs per field of view. Unbound particles were removed by rinsing the channels with 1X PBS (5 × 100 µL).

Each high-throughput assay, was performed in four independent technical replicates, comprised imaging of ~14,400 individual fields of view, corresponding to approximately 0.5-1 million single particles per LNP formulation.

TIRF: High-throughput imaging of single-molecule RNA

Plasma activated glass slides were assembled with sticky-Slide VI 0.4 microfluidic chambers. Fluorescently labeled RNA, diluted in 1X PBS (pH 7.4), was introduced into the channels and incubated for 10 min at room temperature to allow surface immobilization. The RNA concentration was optimized to achieve a low surface density, so as to attain spatially distinct single-molecule. Unbound molecules were removed by washing the channel with 1X PBS (10 × 100 µL). Each experiment was performed in four independent replicates, comprising imaging of ~1200 distinct fields of view.

Live-cell assays

Generation of d2eGFP-expressing cells

HEK293 cells stably expressing destabilized enhanced green fluorescent protein (HEK293- d2eGFP) were established by lentiviral transduction with a vector encoding d2eGFP. Lentiviral particles were generated by co-transfecting HEK293T packaging cells with pMD2.G, psPAX2, and pLV-CMV-d2eGFP plasmids using Lipofectamine 3000 (Thermo Fisher Scientific, Waltham, MA, USA) according to the manufacturer's protocol.

Cell culture

HEK293-d2eGFP cells were cultured in Nunc EasYFlask 25 cm² flasks in Dulbecco's Modified Eagle's Medium (DMEM, 4500 mg/L glucose) supplemented with 2 mM L-glutamine, 1 mM sodium pyruvate, and 10% (v/v) heat-inactivated fetal bovine serum (FBS). Cells were incubated at 37 °C in a humidified incubator with 5% CO_2 and 70% relative humidity and passaged every 3-5 days. All experiments were performed using cells between passages 15 and 20.

Spinning Disk Confocal (SDC) Microscopy: Live-cell d2eGFP knockdown assay

Live-cell imaging was performed on a spinning disk confocal microscope equipped with a 20× air objective lens (Olympus, NA = 0.5), a Prime 95B CMOS camera (Teledyne Photometrics, effective pixel size of 183 nm × 183 nm) and an environmental control chamber (37 °C, 5% CO_2, humidity).

For knockdown assays, cells were seeded at a density of 10,000 cells per well in Ibidi 8-well μ-slides (Ibidi, Martinsried, Germany) containing 200 μL of complete DMEM and incubated for 48 h prior to treatment. Prior to imaging, cells were incubated with 200 μL of imaging medium (phenol red-free DMEM supplemented with 10% FBS) containing LNPs (Supplementary Table 3) encapsulating siRNA targeting eGFP (final concentration 300 nM of encapsulated siRNA), or with imaging medium alone as a negative control. Imaging was initiated 1 h 15 min after LNP addition and continued every 20 min for 24 h. For each condition, 10 positions per well were imaged in parallel. At each position, seven z-plane images were collected with 3 μm spacing using a 488 nm excitation laser at 20% laser power with an exposure time of 50.04 ms. All acquisition settings were kept constant across experiments. Each condition was performed in three independent technical replicates.

Lattice Light-Sheet (LLS) Microscopy

Experiments were performed on a ZEISS Lattice Lightsheet 7 microscope equipped with a 13.3× illumination objective (NA 0.4), a 44.8× detection objective (NA 1.0), and two Hamamatsu ORCA-Fusion sCMOS cameras (6.5 μm pixel size). The light sheet was configured with a $Sinc^3$ profile of 30 × 1000 μm and cropped to 296 μm in width and 43.5 μm in height at a 30° angle, corresponding to 37.1 μm perpendicular to the sample surface. Z-stacks were acquired with a step size of 200 nm. PSF calibration in the Z-direction was performed using fluorescent LNPs in agarose, ensuring a full-width half maximum (FWHM) below 1.0 μm for the 640 nm excitation laser.

LLS: PSF calibration and single-particle characterization

For PSF calibration and single-particle characterization, LNPs were suspended in 1.5% high-melt agarose prepared at 90 °C. A 1:50 dilution of LNP stock was mixed with molten agarose and cast into wells of glass-bottom Ibidi 8-well μ-slides. After cooling to form gels, samples were imaged under the same acquisition settings as live-cell experiments. Immobilized LNPs were excited with a 640 nm laser at either 30% or 100% power (10 ms

exposure). Each condition was recorded in technical triplicates, with each replicate comprising 56 fields of view spanning the full sample well.

LLS: Live-cell internalization assay

For lattice light-sheet microscopy (LLSM) internalization assay, 10,000 cells were seeded into each well of fibronectin-coated (11 µg/mL) glass-bottom Ibidi 8-well µ-slides (Ibidi, Martinsried, Germany) and incubated for 24 h prior to treatment.

Prior to imaging, cells were treated with imaging medium (IMEM) containing either Comp. A N/P 3 LNPs, Comp. B N/P 3 LNPs (Supplementary Table 3), or no LNPs as control for 150 minutes. Following incubation, cells were washed twice with 200 µL imaging medium to remove unbound LNPs and maintained in imaging medium for live-cell imaging.

Live cell imaging was performed at 37°C under 5% CO2, and 70% humidity. LNPs were imaged using a 640 nm laser at 30% or 100% power with a 10 ms exposure time, while cytosolic d2eGFP was excited using a 488 nm laser at 4% power with an exposure time of 10 ms. Each condition was recorded in three independent biological replicates, with 12 fields of view per replicate.

Data analysis and computational experiments

TIRF microscopy data processing and quantitative analysis

Quantitative analysis of single-particle TIRF datasets was performed through a multi-stage image processing pipeline designed to extract physical (Diameters) and molecular parameters (Copies of siRNA) of individual lipid nanoparticles. The workflow included correction for non-uniform illumination, detection and fitting of individual point spread functions (PSFs) to obtain integrated fluorescence intensities, pairwise colocalization of membrane and cargo signals to identify loaded particles, and quantitative conversion of fluorescence values into particle size and siRNA copy number. These steps enabled direct mapping of LNP size to cargo content at single-particle resolution.

Illumination correction

To compensate for spatial variations in excitation intensity across the TIRF field, raw fluorescence movies were corrected using a custom flat-fielding procedure. For each dataset, the mean projection along the temporal axis was smoothed with a Gaussian filter ($\sigma \approx 30$ pixels) and fitted with a two-dimensional Gaussian function combined with a sloped planar background. This composite model captures both the radially decaying excitation characteristic of objective-based TIRF illumination and small linear gradients

introduced by slight beam misalignment or optical throughput variations. Each movie frame was divided by the resulting normalized illumination profile, and the corrected stack was rescaled to preserve the original mean intensity.

Without correction, PSFs located near the edges of the field experience systematically lower apparent brightness compared to those near the center, leading to an artificial broadening of intensity distributions and bias in quantitative single-particle analyses. Applying the illumination correction homogenized the apparent intensity of PSFs across the field of view, enabling accurate comparison of integrated fluorescence values between particles.

Single-particle detection and Gaussian fitting of PSFs

Individual particles were identified in each frame using a GPU-accelerated Laplacian-of-Gaussian–based detector optimized for diffraction-limited features. For every detected particle, a 7 × 7 pixel region (corresponding to 1.12 μm × 1.12 μm at 160 nm px^{-1}) was fitted with a two-dimensional Gaussian function plus a constant background using nonlinear least-squares optimization. This window fully encompasses the expected point-spread function under the imaging conditions.

The fitted parameters included the particle center coordinates (x_0, y_0), the Gaussian widths (σ_x, σ_y), and the amplitude A. From these, the integrated intensity of each particle was calculated as

$$I_{\text{int}} = 2\pi\, A\, \sigma_x \sigma_y,$$

which was used as the sole quantitative descriptor of particle brightness in subsequent analyses. To avoid artifacts from detector saturation, oversaturation masks generated from the raw movies were used to flag particles located within 3 pixels of saturated regions. All results were saved separately for the membrane and cargo channels and used for downstream intensity-based comparisons between individual LNPs.

Colocalization of membrane and cargo particles

To quantify the fraction of LNPs containing encapsulated cargo, colocalization analysis was performed between particles detected in the membrane and cargo fluorescence channels. Each field of view was analyzed pairwise, matching particles based on spatial proximity. Membrane and cargo particle centroids were considered colocalized when their lateral distance was below 1 pixel (160 nm), corresponding to a conservative estimate of the typical localization accuracy expected under the imaging conditions to minimize false positives.

For each LNP formulation and replicate, the total number of membrane particles and the number of colocalized membrane-cargo pairs were quantified. The colocalization fraction was calculated as the ratio of colocalized particles to the total number of membrane-

associated particles. Integrated intensities from the fitted Gaussians were then used to compare the fluorescence distributions of colocalized and non-colocalized populations.

Quantification of siRNA copies per LNP

To quantify siRNA loading per particle, fluorescent intensities were transformed into physical LNP radii and discrete siRNA copy numbers. Colocalization of siRNA with LNPs was first used to identify cargo-bearing particles. Subsequent analysis, apart from the intensity to size conversion in LNPs, was restricted to this subset.

Integrated LNP fluorescence intensity, I, was converted to particle radius, r, using a dynamic light scattering (DLS) anchor. Assuming fluorescence scales with surface area,

$$I \propto r^2$$

the proportionality constant

$$\alpha = \frac{I_{\text{mode}}}{r_{\text{mode}}^2}$$

was defined from the modal intensity of the LNP distribution and the corresponding DLS-derived hydrodynamic radius. Each LNP was then assigned an estimated size:

$$r = \sqrt{\frac{I}{\alpha}}, \ \frac{4}{3}\pi r^3$$

Cargo channel intensities were converted to molecule counts using single-molecule siRNA calibration data, where a gaussian mixture model in log space identified the monomer peak, yielding mean single-molecule intensity I_1. For each particle, siRNA copy number was estimated as

$$N = \frac{e^{\log(I_{\text{cargo}}+1)} - 1}{I_1}$$

This procedure produces a direct mapping of siRNA copy number as a function of LNP radius, enabling quantitative analysis of size-dependent loading.

Extracting multimodal scaling laws

With siRNA counts mapped to LNP radius, 2D histograms revealed distinct ridges of density following different scaling exponents. We first attempted fitting parameterized multi-component distributions directly in the 2D plane, but this approach was unstable. Instead, we adopted a band-wise analysis: LNPs were stratified into narrow radius

intervals, and siRNA copy-number distributions were examined within each band, as depicted in Fig. 3.

Across conditions, siRNA counts within size bands were frequently bimodal. To assess this formally, we fitted one- vs.\ two-component gaussian models in log space and compared them using the Bayesian Information Criterion (BIC). Approximately half of the conditions generally favored size-bands with a two-component fit; the remainder were best described by a single gaussian.

Scaling laws were therefore evaluated in two complementary ways:

(a) the mean siRNA count per LNP radius (robust to uni- or bimodality), and

(b) separate scaling exponents for “high-load” and “low-load” subpopulations, by tracking which gaussian corresponded to the higher vs. lower siRNA peak within each radius band.

Simulating scaling laws via stochastic LNP mergers

To interpret observed scaling of siRNA loading as a function of LNP size, we implemented a stochastic coagulation model representing the dynamic formation of LNPs through successive binary mergers. Each event corresponds to the fusion of two lipid domains, consistent with proposed LNP self-assembly mechanisms based on progressive domain coalescence[44,45]. The process is simulated as an asynchronous, event-driven system following Gillespie dynamics, ensuring a realistic evolution of the particle size distribution over time.

At the initial time point $(t = 0)$, N_0 spherical LNPs are generated with radii drawn from a normal distribution $(r_0 \pm \sigma_r)$. Each particle is assigned a discrete siRNA cargo, initialized according to a Bernoulli distribution that determines the encapsulation fraction:

$$C_i(0) \sim \text{Bernoulli}(p_{\text{load}})$$

where p_{load} defines the initial probability that an LNP contains siRNA (i.e., $1 - p_{\text{load}}$ is the empty fraction).

At each stochastic event, two particles, i and j, are selected uniformly at random and merged into a new particle. The resulting LNP inherits its physical and cargo properties through additive combination: $V_{\text{new}} = V_i + V_j, \qquad C_{\text{new}} = C_i + C_j, \qquad r_{\text{new}} = \left(\frac{3V_{\text{new}}}{4\pi}\right)^{1/3}$

The merged particle replaces the two parent particles in the active population, and the process continues until the largest particle reaches a predefined hydrodynamic radius ($r_{\text{max}} = 1500$nm), corresponding to the upper experimental size regime. Volume-additivity was selected as electron-microscopy indicated that the lipids aggregate in a manner consistent with volumetric coordination.

The remaining particles at this stopping point represent the terminal distribution of LNP sizes and siRNA copy numbers, $p_\tau(r, C)$, at time τ. This ensemble provides a synthetic counterpart to experimentally measured populations, where individual nanoparticles are observed after assembly rather than during formation.

From this terminal distribution, the empirical relationship between siRNA count and LNP radius is determined by fitting a power law of the form

$$C(r) = a\,r^b$$

where b denotes the effective scaling exponent. For homogeneous seeding and conserved cargo, b approaches 3, reflecting volume-proportional loading. Under sparse encapsulation ($p_{\text{load}} \ll 1$), the effective exponent decreases, typically near $b \approx 1.2$ to $b \approx 2.1$ for $p_{\text{load}} = 0.05$ to $p_{\text{load}} = 0.2$, respectively, consistent with experimental measurements. This deviation from direct volumetric scaling arises naturally from stochastic variations in merger history and the low frequency of cargo-bearing progenitors, without requiring any explicit cargo loss or surface-limited loading assumptions. Our computational coalescence modeling as such aims to interpret where the observed scaling exponents arise from. While a uniform kernel, that is the probability of any two particles merging is the same for any other, does not explain the observed heterogeneity in scaling for some conditions, we are able to theorize that the sub-volume proportional cargo loading may very well arise from the initial encapsulation efficiency.

Live-cell quantification of siRNA-mediated eGFP knockdown following LNP delivery

Knockdown kinetics were quantified from time-lapse fluorescence measurements acquired by spinning-disk confocal microscopy. For each well and imaging position, seven z-planes (3 µm spacing) were acquired and collapsed by maximum-intensity projection. Cells were segmented on maximum-intensity projections of the eGFP channel together with a user-selected brightfield z-plane to improve boundary detection when fluorescence was low after knockdown.

Within each field of view (FOV) and frame, mean cellular eGFP intensity was computed per segmented cell; these per-cell values were averaged to yield an FOV-level mean for that frame. For a given replicate and frame, the replicate-level mean was then obtained by averaging the FOV-level means across all FOVs imaged for that replicate. This produced one time series per replicate, $T_i(t)$, sampled every 20 min for ~24 h after LNP treatment.

To construct a global reference trajectory for untreated controls, all control replicates from the same experiment were pooled to form $C(t)$, the inverse-variance–weighted mean of per-replicate control curves:

$$C(t) = \frac{\sum_j w_j(t)\, C_j(t)}{\sum_j w_j(t)}, w_j(t) = \frac{1}{\sigma_j^2(t)},$$

where $C_j(t)$ and $\sigma_j(t)$ denote the mean and standard deviation of the control replicate j at time t. The pooled control trajectory captures the shared recovery and bleaching dynamics of untreated cells.

Each treated replicate $T_i(t)$ was normalized to the control by first estimating a scalar baseline-alignment factor s_i that minimized the least-squares difference to $C(t)$ over the initial "no-effect" window (within the first hour):

$$s_i = \frac{\sum_{t \in \mathcal{W}_{\text{baseline}}} T_i(t)\, C(t)}{\sum_{t \in \mathcal{W}_{\text{baseline}}} T_i^2(t)}.$$

The aligned trace was

$$T_i^{\text{aligned}}(t) = s_i\, T_i(t),$$

and the normalized signal ratio

$$S_i(t) = \frac{T_i^{\text{aligned}}(t)}{C(t)}$$

was computed at all shared time points. By construction, $S_i(t) \approx 1$ at early times and decreases when eGFP expression is suppressed relative to control.

To suppress frame-to-frame noise and enforce the expected monotonic decline of fluorescence as siRNA knockdown progresses, $S_i(t)$ was first smoothed with a moving-average filter and then projected onto a monotone non-increasing function using isotonic regression. When available, propagated per-timepoint uncertainties were used as weights in the fit. The resulting piecewise-constant curve $S_i^{\text{mono}}(t)$ represents the denoised knockdown trajectory for that replicate.

From $S_i^{\text{mono}}(t)$, the maximum knockdown was calculated as:

$$KD_i = 100 \times (1 - \min_t S_i^{\text{mono}}(t)),$$

reflecting the largest fractional decrease in eGFP intensity relative to control. All analyses were performed independently per replicate (one well). Replicate-level values were summarized per LNP formulation as mean ± SEM.

Quantification of internalized LNPs per cell

To quantify the average number of internalized LNPs per cell, 3D fluorescence volumes acquired in the lattice light-sheet microscopy (LLSM) assay were analyzed across all biological replicates. Endosomes can undergo rapid fusion and fission that can result in in multiple LNPs per endosome. This consequently challenges quantitative extraction of the LNP number per cell. To extract therefore an estimate of the number of LNPs internalized per cell we quantified the total background-corrected cellular fluorescence of LNPs in cells and divided with the corresponding mean single-LNP intensity.

Cells expressed cytosolic d2eGFP, which was used for segmentation of individual cellular volumes. A representative z-slice containing well-separated cells was segmented using Cellpose-SAM, and segmentation was propagated across the remaining z-slices using SAM2 by interpreting each slice as a temporal variation of the reference plane. The resulting masks were combined to generate a 3D cell volume for each cell.

For each cell, the mean per-voxel fluorescence intensity of the LNP channel was measured within the segmented volume. These per-cell values were then averaged across all cells within each biological replicate to obtain the replicate-level mean per-voxel fluorescence intensity. The same analysis was applied to control samples (no-LNP) to determine cellular background fluorescence. The background-corrected LNP-associated intensity per voxel was then obtained by subtracting, for each replicate, the mean per-voxel intensity measured in the control condition from that measured in the corresponding experimental condition. The resulting background-corrected intensity was summed across all voxels within each cell, yielding the total fluorescence associated with internalized LNPs.

Single-particle calibration was performed using immobilized LNPs embedded in 1.5% high-melt agarose and imaged under identical acquisition conditions. Particles were detected using a Crocker-Grier-based 3D detection algorithm, and each detection was fitted with a 3D Gaussian model to obtain the integrated fluorescence intensity. The mean integrated intensity of isolated LNPs was used as the reference brightness of a single particle for each formulation.

For each experimental condition, the total background-corrected cellular fluorescence was divided by the corresponding mean single-LNP intensity, providing an estimate of the number of LNPs internalized per cell. The resulting values were averaged across all cells within each biological replicate, and the final mean and standard error of the mean (SEM) were computed across replicates.

References

1. Hou, X., Zaks, T., Langer, R. & Dong, Y. Lipid nanoparticles for mRNA delivery. *Nat. Rev. Mater.* **6**, 1078–1094 (2021).
2. Gilleron, J. *et al.* Image-based analysis of lipid nanoparticle–mediated siRNA delivery, intracellular trafficking and endosomal escape. *Nat. Biotechnol.* **31**, 638–646 (2013).
3. Dowdy, S. F. Overcoming cellular barriers for RNA therapeutics. *Nat. Biotechnol.* **35**, 222–229 (2017).
4. Schlich, M. *et al.* Cytosolic delivery of nucleic acids: The case of ionizable lipid nanoparticles. *Bioeng. Transl. Med.* **6**, (2021).
5. Dowdy, S. F., Setten, R. L., Cui, X.-S. & Jadhav, S. G. Delivery of RNA Therapeutics: The Great Endosomal Escape! *Nucleic Acid Ther.* **32**, 361–368 (2022).
6. Dowdy, S. F. Endosomal escape of RNA therapeutics: How do we solve this rate-limiting problem? *RNA* **29**, 396–401 (2023).
7. Aliakbarinodehi, N. *et al.* Time-Resolved Inspection of Ionizable Lipid-Facilitated Lipid Nanoparticle Disintegration and Cargo Release at an Early Endosomal Membrane Mimic. *ACS Nano* **18**, 22989–23000 (2024).
8. Sahay, G. *et al.* Efficiency of siRNA delivery by lipid nanoparticles is limited by endocytic recycling. *Nat. Biotechnol.* **31**, 653–658 (2013).
9. Johansson, J. M. *et al.* Cellular and biophysical barriers to lipid nanoparticle mediated delivery of RNA to the cytosol. *Nat. Commun.* **16**, (2025).

10. Uebbing, L. *et al.* Investigation of pH-Responsiveness inside Lipid Nanoparticles for Parenteral mRNA Application Using Small-Angle X-ray Scattering. *Langmuir* **36**, 13331–13341 (2020).
11. Yu, H. *et al.* Real-Time pH-Dependent Self-Assembly of Ionisable Lipids from COVID-19 Vaccines and In Situ Nucleic Acid Complexation. *Angew. Chem. Int. Ed.* **62**, (2023).
12. Kulkarni, J. A. *et al.* On the Formation and Morphology of Lipid Nanoparticles Containing Ionizable Cationic Lipids and siRNA. *ACS Nano* **12**, 4787–4795 (2018).
13. Liu, L. *et al.* PEGylated lipid screening, composition optimization, and structure–activity relationship determination for lipid nanoparticle-mediated mRNA delivery. *Nanoscale* **17**, 11329–11344 (2025).
14. Zheng, L., Bandara, S. R., Tan, Z. & Leal, C. Lipid nanoparticle topology regulates endosomal escape and delivery of RNA to the cytoplasm. *Proc. Natl. Acad. Sci.* **120**, e2301067120 (2023).
15. Yu, H. *et al.* Inverse Cubic and Hexagonal Mesophase Evolution within Ionizable Lipid Nanoparticles Correlates with mRNA Transfection in Macrophages. *J. Am. Chem. Soc.* https://doi.org/10.1021/jacs.3c08729 (2023) doi:10.1021/jacs.3c08729.
16. Spadea, A. *et al.* Nucleic Acid-Loaded Lipid Nanoparticle Interactions with Model Endosomal Membranes. *ACS Appl. Mater. Interfaces* **14**, 30371–30384 (2022).
17. Mo, Y. *et al.* Lipid-siRNA Organization Modulates the Intracellular Dynamics of Lipid Nanoparticles. *J. Am. Chem. Soc.* **147**, 10430–10445 (2025).
18. Pattipeiluhu, R. *et al.* Liquid crystalline inverted lipid phases encapsulating siRNA enhance lipid nanoparticle mediated transfection. *Nat. Commun.* **15**, 1303 (2024).

19. Zhang, J., Haas, R. M. & Leone, A. M. Polydispersity Characterization of Lipid Nanoparticles for siRNA Delivery Using Multiple Detection Size-Exclusion Chromatography. *Anal. Chem.* **84**, 6088–6096 (2012).
20. Peretz Damari, S. *et al.* Practical aspects in size and morphology characterization of drug-loaded nano-liposomes. *Int. J. Pharm.* **547**, 648–655 (2018).
21. Henrickson, A. *et al.* Density Matching Multi-wavelength Analytical Ultracentrifugation to Measure Drug Loading of Lipid Nanoparticle Formulations. *ACS Nano* **15**, 5068–5076 (2021).
22. Crawford, R. *et al.* Analysis of lipid nanoparticles by Cryo-EM for characterizing siRNA delivery vehicles. *Int. J. Pharm.* **403**, 237–244 (2011).
23. Li, S. *et al.* Single-Particle Spectroscopic Chromatography Reveals Heterogeneous RNA Loading and Size Correlations in Lipid Nanoparticles. *ACS Nano* **18**, 15729–15743 (2024).
24. Sjöberg, M. *et al.* Multiparametric functional characterization of individual lipid nanoparticles using surface-sensitive light-scattering microscopy. *Proc. Natl. Acad. Sci.* **122**, e2426601122 (2025).
25. Padilla, M. S. *et al.* Elucidating lipid nanoparticle properties and structure through biophysical analyses. *Nat. Biotechnol.* 1–14 (2025) doi:10.1038/s41587-025-02855-x.
26. Malle, M. G. *et al.* Single-particle combinatorial multiplexed liposome fusion mediated by DNA. *Nat. Chem.* **14**, 558–565 (2022).
27. Thomsen, R. P. *et al.* A large size-selective DNA nanopore with sensing applications. *Nat. Commun.* **10**, 5655 (2019).

28. Schmidt, S. G. *et al.* The dopamine transporter antiports potassium to increase the uptake of dopamine. *Nat. Commun.* **13**, 2446 (2022).

29. Hatzakis, N. S. *et al.* How curved membranes recruit amphipathic helices and protein anchoring motifs. *Nat. Chem. Biol.* **5**, 835–841 (2009).

30. Stella, S. *et al.* Conformational Activation Promotes CRISPR-Cas12a Catalysis and Resetting of the Endonuclease Activity. *Cell* **175**, 1856-1871.e21 (2018).

31. Jensen, S. B. *et al.* Biased cytochrome P450-mediated metabolism via small-molecule ligands binding P450 oxidoreductase. *Nat. Commun.* **12**, 2260 (2021).

32. Udepurkar, A. *et al.* Structure and Morphology of Lipid Nanoparticles for Nucleic Acid Drug Delivery: A Review. *ACS Nano* **19**, 21206–21242 (2025).

33. Rode García, T. *et al.* Unified Scaling of the Structure and Loading of Nanoparticles Formed by Diffusion-Limited Coalescence. *Langmuir* **34**, 5772–5780 (2018).

34. Gindy, M. E. *et al.* Mechanism of Macromolecular Structure Evolution in Self-Assembled Lipid Nanoparticles for siRNA Delivery. *Langmuir* **30**, 4613–4622 (2014).

35. Kulkarni, J. A. *et al.* Fusion-dependent formation of lipid nanoparticles containing macromolecular payloads. *Nanoscale* **11**, 9023–9031 (2019).

36. Kæstel-Hansen, J. *et al.* Deep learning-assisted analysis of single-particle tracking for automated correlation between diffusion and function. *Nat. Methods* **22**, 1091–1100 (2025).

37. Huang, G. *et al.* Defect-Engineered Metal–Organic Frameworks as Nanocarriers for Pharmacotherapy: Insights into Intracellular Dynamics at The Single Particle Level. *Adv. Mater.* **36**, 2405898 (2024).

38. Escalona-Rayo, O. *et al*. *In vitro* and *in vivo* evaluation of clinically-approved ionizable cationic lipids shows divergent results between mRNA transfection and vaccine efficacy. *Biomed. Pharmacother.* **165**, 115065 (2023).

39. Cavegn, A. *et al*. Intracellular processing of DNA-lipid nanoparticles: A quantitative assessment by image segmentation. *J. Controlled Release* **382**, 113709 (2025).

40. Pei, D. Endosomal Escape of Lipid Nanoparticles: A New Perspective on the Literature Data. Preprint at https://doi.org/10.26434/chemrxiv-2025-t8115 (2025).

41. Muzzopappa, F., Hertzog, M. & Erdel, F. DNA length tunes the fluidity of DNA-based condensates. *Biophys. J.* **120**, 1288–1300 (2021).

42. Pérez-Illana, M. *et al*. Acidification induces condensation of the adenovirus core. *Acta Biomater.* **135**, 534–542 (2021).

43. Sanyal, A. *et al*. Neuronal constitutive endolysosomal perforations enable α-synuclein aggregation by internalized PFFs. *J. Cell Biol.* **224**, e202401136 (2024).

44. Shin, S. *et al*. Mechanistic modeling of lipid nanoparticle (LNP) precipitation via population balance equations (PBEs). *Chem. Eng. J.* **523**, 167786 (2025).

45. Inguva, P. K. *et al*. Mechanistic modeling of lipid nanoparticle formation for the delivery of nucleic acid therapeutics. *Biotechnol. Adv.* **84**, 108643 (2025).